

# Low-voltage FIB/SEM Tomography for 3D Microstructure Evolution of LiFePO4/C Electrode

**Scipioni, Roberto; Jørgensen, Peter Stanley; Ngo, Duc-The; Simonsen, Søren Bredmose; Hjelm, Johan; Norby, Poul; Jensen, Søren Højgaard**

*Published in:*
E C S Transactions

*Link to article, DOI:*
10.1149/06918.0071ecst

*Publication date:*
2015

*Document Version*
Peer reviewed version

# Low-voltage FIB/SEM Tomography for 3D Microstructure Evolution of $LiFePO_4$/C Electrode

R. Scipioni, P. S. Jørgensen, D. T. Ngo, S. B. Simonsen, J. Hjelm, P. Norby, and S. H. Jensen

Department of Energy Conversion and Storage, Technical University of Denmark, DTU Risø Campus, Frederiksborgvej 399, 4000 Roskilde, Denmark

This work presents an investigation of the degradation mechanisms that occur in $LiFePO_4$/C battery electrodes during charge/discharge cycling. Impedance spectra were measured on a fresh electrode and an electrode aged by cycling. The spectra were modeled with an equivalent circuit which indicates that both the ionic and electronic pathways in the electrode were negatively affected by the cycling. Focused Ion Beam/Scanning Electron Microscopy (FIB/SEM) tomography of both electrodes shows that cycling causes agglomerations of Carbon black (CB). In addition to this, Low-voltage FIB/SEM revealed non-conductive CB in the aged electrode.

## Introduction

Li-ion batteries find widespread use in many applications, from portable devices to electric vehicles [1-3], and $LiFePO_4$ (LFP) is one of the most common cathode materials because of its long durability and high safety [4, 5]. Since LFP is a poor electronic conductor, it is always mixed with carbon black (CB) additives to increase electronic percolation in the electrode. LFP is known to be subjected to expansion/contraction with cycling. The resulting mechanical stress leads to formation of micro-cracks inside the LFP particles [6-8] and aggregation of CB [9]. FIB/SEM tomography is one of the most used techniques for quantitative observations of electrode morphology and structure [10-12]. SEM imaging at low-kV has previously been used to study electron percolation in solid oxide fuel cell Ni/YSZ-electrodes [13]. Here we combine low-kV SEM imaging with FIB to study electron percolation in three dimensions (3D) in two laboratory $LiFePO_4$/C electrodes; one fresh and one degraded by cycling. A loss of electron percolation was observed in the degraded electrode, correlating with modeling of impedance spectra recorded on the two electrodes.

## Experimental

### Cell assembly and testing

The electrodes were prepared by casting, on aluminum foil, a slurry made of commercial $LiFePO_4$ powder (already carbon coated, from MTI), Super C65 carbon black (from Timcal) and Polyvinylidene Fluoride (PVdF) as binder, with the ratio 80:10:10. After drying, two electrodes with a diameter of 18 mm and thickness of 22 μm

were punched out. The electrodes were tested in an EL-CELL® ECC-Combi 3-electrode setup, using lithium metal foil counter electrodes, lithium metal as reference electrode and a glass fiber separator soaked with a standard 1M $LiPF_6$ in 1:1 EC/DMC electrolyte. Both cells were cycled at constant C-rate using a Biologic VMP3 with Pstat/Gstat boards. Table 1 shows the test conditions for the two electrodes.

**TABLE I.** Test conditions.

| Electrode | Current (mA $g^{-1}$) | Voltage limits | Total cycle number | Remaining capacity |
|---|---|---|---|---|
| Fresh | 17 | 3 – 4 V | 2 | ~ 100% |
| Aged | 17 | 3 – 4 V | 100 | ~ 30% |

Impedance spectroscopy

The 3-electrode setup combined with the Biologic VMP3 enabled electrochemical impedance spectroscopy (EIS) measurements of the $LiFePO_4$/C electrodes. EIS measurements in a frequency range from 100 kHz to 10 mHz of both the fresh and the aged electrode were obtained after discharging the cells at 3V with a calculated 0.1 C-rate. All measurements were performed at OCV after the cell had reached steady state defined by a change < 5 mV/h. The impedance results were modeled using the equivalent circuit presented in Fig. 1.

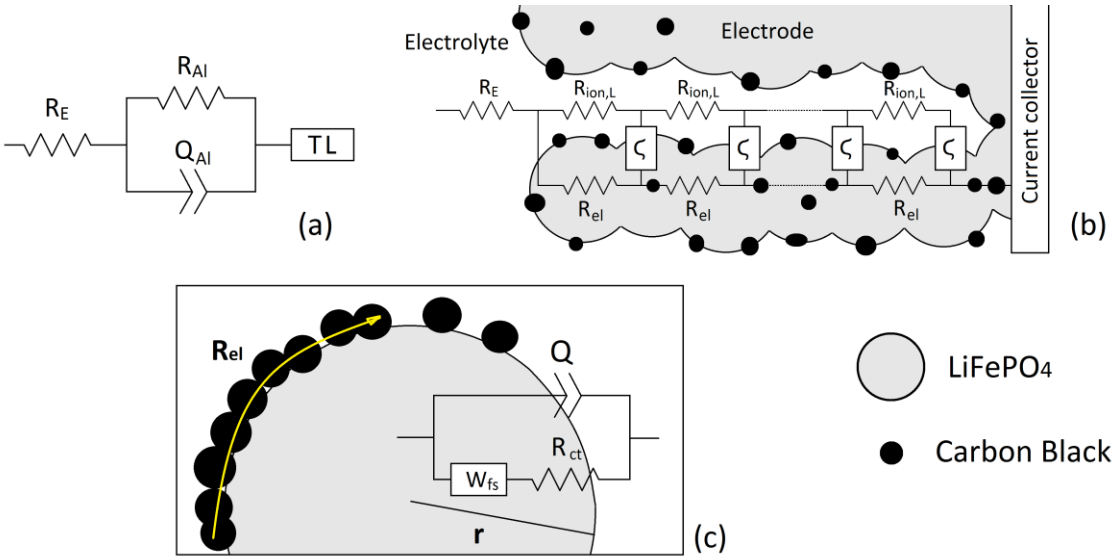


**Figure 1. (a)** Equivalent circuit used to model the impedance spectra, **(b)** Generalized Transmission Line model resembling the element TL in (a), **(c)** Randles circuit used to model electrode/electrolyte interface with $Li^+$ diffusion (Warburg Finite Space element, $W_{fs}$) within a particle with radius $r$. The Randles circuit resembles the element $\zeta$ in (b). The yellow arrow in (c) indicates the electron pathway on the surface of the LFP particle.

The $R_E$-$R_{Al}Q_{Al}$ elements, Fig. 1(a) model the high-frequency region where $R$ corresponds to a resistance and $Q$ corresponds to a constant phase element. $R_E$ represents the ionic resistance of the electrolyte, while the $R_{Al}Q_{Al}$ element denotes the aluminum/electrode polarization impedance [14]. The low-frequency region was modeled with a generalized transmission line (TL) for a porous electrode [15-17], Fig. 1(b). This model involves a cylindrical pore (filled with the electrolytic solution) with length $L$,

electronic resistance of the electrode $R_{el}$, ionic resistance of the solution in the pore $R_{ion,L}$ and an equivalent circuit $\zeta$ to model the interface electrode/electrolyte, including charge transfer resistance, double layer capacitance and solid state diffusion. The electronic resistance is often assumed to be much lower than the ionic resistance of the solution ($R_{el}$<<$R_{ion,L}$) for which reason a simplified transmission line without the electronic rail is used [17, 18]. However, assuming to find a higher $R_{el}$ non-negligible electronic resistance in the aged electrode, the generalized version of the transmission line model is used [15-17], where the overall impedance is:

$$Z_{TL} = \frac{R_{el} * R_{ion,L}}{R_{el} + R_{ion,L}}\left(L + \frac{2\lambda}{\sinh(L/\lambda)}\right) + \lambda\frac{R_{el}^2 + R_{ion,L}^2}{R_{el} + R_{ion,L}}\coth(L/\lambda) \quad [1]$$

With:

$$\lambda = \sqrt{\zeta/\left(R_{el} + R_{ion,L}\right)} \quad [2]$$

The electrode/electrolyte interface, Fig. 1(c), has been modeled with a Randles circuit which includes the charge transfer resistance $R_{ct}$, a constant phase element $Q$ (from which the effective double layer capacitance $C_{dl}$ is calculated according to [19]) and the general finite space Warburg element $W_{GFS}$ [20-22], with the impedance:

$$Z_{WGFS} = R_w\frac{\coth[(j\omega\tau_w)^{n_w}]}{(j\omega\tau_w)^{n_w}} \quad [3]$$

With time constant:

$$\tau_w = \frac{r^2}{D} \quad [4]$$

$R_w$ is polarization resistance, $n_w$ is an exponent ($0<n_w<0.5$), $r$ is the particle radius and $D$ is the diffusion coefficient of Lithium ion within $LiFePO_4$.

FIB/SEM Tomography

FIB tomography and SEM imaging was carried out on a Zeiss 1540XB CrossBeam microscope, using a lateral E-T (Everhart-Thornley) detector and an In-lens detector. Two 3D datasets were collected from the fresh electrode (labeled as F1 and F2) and three from the aged one (labeled as A1, A2 and A3). Table 2 shows the volume sizes of the 5 different 3D datasets. A gallium FIB slicing probe of 2nA was used and the thickness of each slice was estimated to be 40 nm. The serial sectioning imaging was performed at 1 kV with a pixel size of 15x15 $nm^2$, and the voxel size in the five 3D-data sets was therefore 40x15x15 $nm^3$. The electrodes were prepared for FIB tomography by rinsing with diethyl carbonate and vacuum infiltrated with a silicon resin (Wacker Chemie) for 30 minutes to improve phase contrast between CB particles and pores as described by Ender et al [11]. Subsequently the samples were infiltrated with epoxy resin to enable high-quality grinding and polishing of the sample.

**TABLE II.** Volumes of collected datasets.

| Dataset | Volume (voxels) X x Y x Z | Volume (µm3) X x Y x Z |
|---|---|---|
| F1 | 250 x 683 x 341 | 10 x 10 x 5 |
| F2 | 141 x 683 x 341 | 5.6 x 10 x 5 |
| A1 | 250 x 683 x 341 | 10 x 10 x 5 |
| A2 | 131 x 683 x 341 | 5.2 x 10 x 5 |
| A3 | 150 x 683 x 341 | 6 x 10 x 5 |

Low-voltage FIB/SEM

The low-voltage SEM technique has previously been used to study electron percolation by Thydén et al [13] and is here combined with a FIB to study the three-dimensional electron percolation in the CB network.

A low accelerating voltage (in our case 1 kV) causes a high secondary electron (SE) yield thereby charging the investigated specimen (depending on the examined material) [23, 24]. For electron conducting phases with a connection to ground, the local buildup of charge is rapidly equalized and no charging effects are observed. For insulators, the lack of charge dissipation means that a 1-1 balance between ingoing and outgoing electrons is rapidly established, mainly through charging of the insulator since the charging results in deflection/attraction of electrons. The silicon resin used to infiltrate the specimens (to fill out pores in the electrode) has a total electron yield higher than 1 [23, 24], meaning that it is expected to charge positively and appear bright, when imaged at 1 kV.

Electron conducting carbon was observed to be darker than non-electron-dissipating carbon particles, indicating that the later carbon type tends to charge positively.

Image processing

Segmentation and statistical data analysis of the 3D FIB/SEM image data was performed with the program ImageJ (NIH). Because of uneven illumination, setting a single threshold for entire micrographs was not feasible. Therefore the Sauvola algorithm [25, 26] was used to perform local thresholds of the data. The Sauvola algorithm works by dividing the input image into square windows (n x n pixel) and setting thresholds for each of them based on the mean and standard deviation of the pixel intensities. Visualizations of the 3D reconstructions of the data were performed with the program Avizo (FEI).

## Results

Impedance spectra modeling

The normalized[1] impedance of the fresh electrode (dots) with the modeling result (line) using the model presented above is shown in Fig. 3(a,b). The Nyquist plot, Fig. 3(a), consists of a small semicircle in the high frequency range (between 10 kHz and 10 Hz) and a low frequency branch characterized by a diffusive tail (with an angle close to 45°). Modelling values are given in Table 3.

[1] Normalized to the geometrical surface area 2.545 $cm^2$

The high frequency side of the semicircle intersects with the x-axis at 9 $\Omega cm^2$ ($R_E$). This value originates mainly from the ionic resistance of the electrolyte between the cathode and the Li reference electrode. As mentioned above, the semicircle ($R_{Al}Q_{Al}$) can be assigned to the interface between the Aluminum current collector and the porous cathode [14], where $R_{Al}$ corresponds to the contact resistance between current collector and the $LiFePO_4$/C network, while $Q_{Al}$ is the constant phase element which represents the double layer capacitance at this interface. The effective double layer capacitance $C_{Al}$ is subsequently calculated [19] and presented in Table 3. The low-frequency part (TL) of the Nyquist plot models the electrode/electrolyte interface (with $R_{ct}$, $C_{dl}$ and Finite Space Warburg diffusion of $Li^+$ ions inside the LFP particle with radius $r$) [20-22] including the electron resistivity through the Carbon Black and the ion resistivity into the pore (with lenght $L$) filled with the electrolyte [15-17]. The LFP particle radius used in this fitting are 55 and 40 nm for fresh and aged electrode respectively, while the pore length $L$ is 22 μm. The particle size values were obtained by particle size distribution analysis reported elsewhere [28].

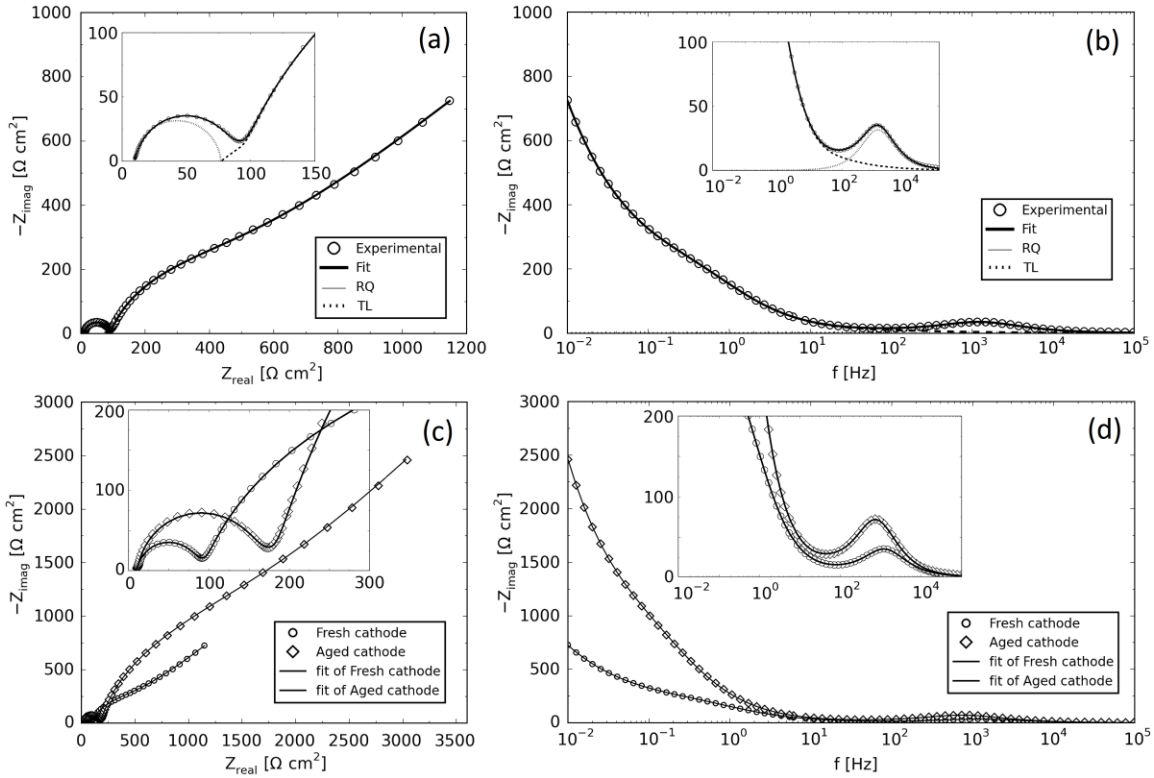


Figure 2. (a) Nyquist and (b) Bode plot of the fresh electrode at 0% SOC including fit using the equivalent circuit in equation 1. (c) Nyquist and (d) Bode plot of fresh and aged electrode at 0% SOC. The EIS measurements are performed after discharging the electrodes at 3V, at OCV after relaxation. All insets show a zoomed view of the high frequency region.

Figure 2 (c,d) shows the impedance response of both fresh and aged electrodes at the discharged state. Comparing the two impedance response is possible to observe an increase in the size of the first semicircle and of the transmission line. As seen in Table 3, the modelling suggests that these increases are mainly due to a raise in the electric and the ion resistivity in the porous electrode.

**TABLE III.** Results from EIS fitting.

| | RQ element | | Transmission Line | | | | |
|---|---|---|---|---|---|---|---|
| | $R_{Al}$ ($\Omega cm^2$) | $C_{Al}$ ($\mu F$) | $R_{ct}$ ($\Omega cm^2$) | $C_{dl}$ ($F$) | $D$ ($cm^2 s^{-1}$) | $R_{ion,L}$ ($\Omega cm^{-1}$) | $R_{el}$ ($\Omega cm^{-1}$) |
| Fresh | 68 | 4.2 | 0.66 | 0.75 | $2.7 \cdot 10^{-11}$ | 8760 | 21 |
| Aged | 142 | 3 | 3.27 | 0.64 | $2.9 \cdot 10^{-11}$ | 17260 | 1546 |

The aged electrode shows a big rise in the contact resistance $R_{Al}$ between current collector and porous electrode and slight decrease in double layer capacitance $C_{dl}$. The charge transfer resistance $R_{ct}$ at the interface between electrode material and electrolyte, is observed to be higher in the aged electrode than in the fresh electrode, while $C_{dl}$ is smaller. As expected, the $Li^+$ ion diffusion coefficient was relatively constant, and it is in agreement with value found in literature [27]. Interestingly, the ionic resistance is seen to double, while the electron resistance within carbon black additive drastically increases.

Low-voltage FIB/SEM

Figure 3 shows SEM images after FIB slicing, recorded at low accelerating voltage (1 kV), of the fresh electrode (region F2, Fig 3(a,b)) and of the aged electrode region A2, Fig. 3(c,d). SEM images of other regions are reported by *Scipioni et al* [28]. The images were recorded with E-T detector Fig. 3(a,c) and with the In-lens detector Fig. 3(b,d).

In the images recorded at 1 kV with the E-T detector Fig. 3 (a,c) we can observe a very bright area on the top, which is the electrode surface. It is possible to distinguish three different phases: the grains with the brightest contrast are LFP particles, the almost black regions are CB and the large grey areas in-between are pores filled with silicon resin. The fresh electrode, Fig. (3a) shows a relatively homogeneous distribution of sub-micrometer LFP grains and CB particles. On the contrary, the aged sample (Fig. 3c) has a less homogeneous distribution of both LFP and CB and an increased porosity. The aged sample is further characterized by the presence of larger CB agglomerates surrounding some LFP grains, which is not observed in the fresh electrode.

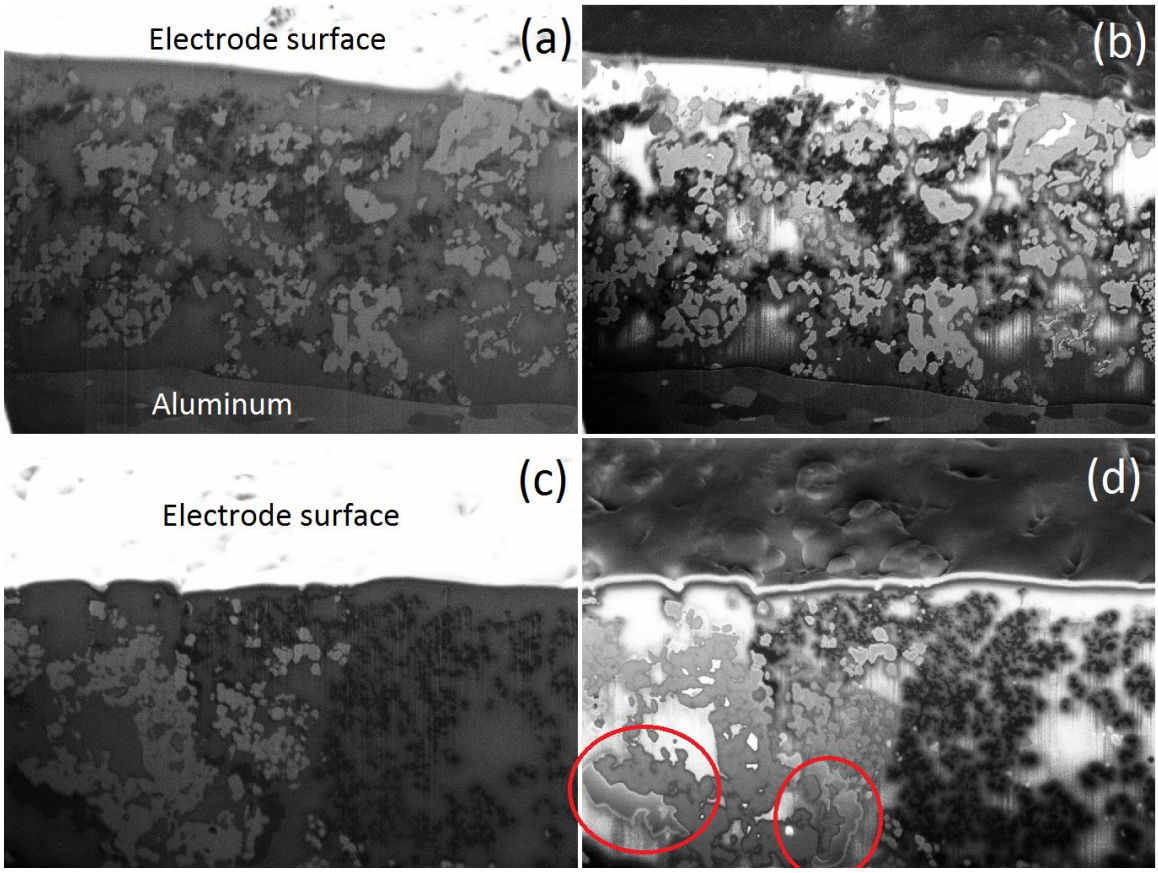

Figure 3. SEM images at 1 kV of the (a,b) fresh and (c,d) aged electrode recorded with the (a,c) Lateral E-T and (b,d) In-lens detector.

In the images recorded at 1 kV with the In-lens detector it can be observed that the silicon resin has high intensity in the parts of the sample not adjacent to electron conducting phases. This indicates that the silicon resin is charging negatively due to low conductivity to the ground. The CB network is instead expected to have a good conductivity and connectivity to the ground. Consistent with this expectation, the CB in the fresh sample has a dark contrast, which indicates minimal charging Fig. (3b). However, in the aged electrode on Fig. (3d) large agglomerations (circled in red) of what appears to be CB are brighter than other CB regions. This indicates that those agglomerations are charging negatively i.e. have lost connection to ground and/or have low conductivity. In other words, these CB regions appear not to be electron percolating.

3D Reconstruction

The SEM images, recorded after FIB slicing from the five dataset F1, F2, A1, A2 and A3 have been used for three dimensional reconstructions. Fig 4 shows a volume rendering of the 3D FIB tomography reconstruction after image segmentation of the 1 kV Lateral E-T image dataset from F2 and A2. Other 3D reconstructions can be found in [28]. From the figure it can be observed that all phases are less homogeneously distributed in A2 in all three dimensions, and not only in the single slice presented in fig. 2. Furthermore large CB agglomerates are seen in the aged electrode [28].

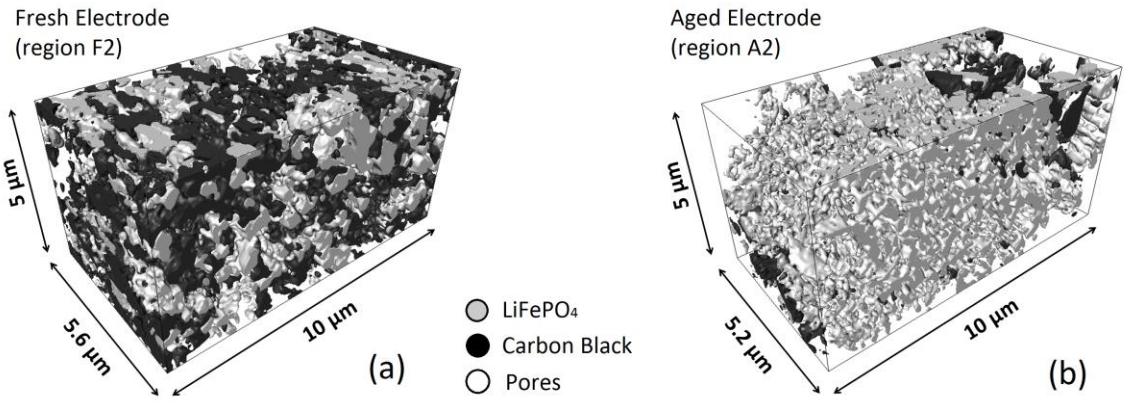


Figure 4. Volume rendering of the 3D reconstruction of a) fresh and b) aged electrode, after segmentation of Lateral E-T images.

The segmented regions from the 5 dataset have been used to extract and calculate statistical data. Table 4 shows the calculated phase fraction for all the volumes. Furthermore the average LFP particles size for the fresh and the aged electrode were calculated equal to 110 and 80 nm, respectively. More results from the particle size distribution analysis can be found in [28].

**TABLE IV.** Phase volume fraction for fresh and aged electrode.

| **Phase** | **F1** | **F2** | **Fresh (Av. and Deviation)** | **A1** | **A2** | **A3** | **Aged (Av. and Deviation)** |
|---|---|---|---|---|---|---|---|
| $LiFePO_4$ | 23% | 17% | 20% ± 3% | 12% | 18% | 12% | 14% ± 3% |
| CB | 16% | 15% | 15.5% ± 0.5% | 16% | 5% | 26% | 16% ± 9% |
| Pores | 61% | 68% | 64.5% ± 3.5% | 72% | 77% | 62% | 70% ± 6% |

As described in relation to Fig. 2, by using the images recorded by the In-lens detector for 3D segmentation we can distinguish between percolating and non-percolating CB. Fig. 5 shows a volume rendering of the 3D reconstruction of the CB network in F2 and A2. The amount of non-percolating CB was 29% in A2 and 0% in F2.

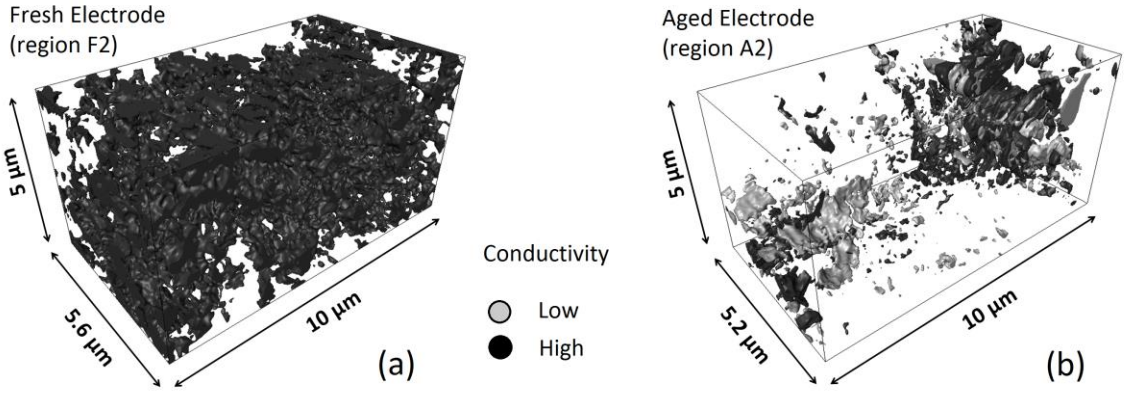


Figure 5. Volume rendering of the 3D reconstruction of a) fresh and b) aged carbon network, after segmentation of In-lens images.

## Discussion

The impedance spectra modeling, indicates that most of the electrode degradation is due to changes in morphology and electrical conductivity of CB additive. Presence of low-conductive carbon, as shown by low-voltage FIB/SEM tomography, is clearly found to lead to an increase in electric resistivity both at the aluminum/electrode interface and throughout the CB network. This is suggested by the rise in $R_{Al}$ in the first semicircle in the aged electrode. The drop in $C_{dl}$ is also expected after CB agglomeration, having a smaller surface in contact between the CB network and the current collector, and being $C_{dl}$ directly proportional to the surface area. The lithium ion $R_{ct}$ is also found to increase in the Randles circuit which models the electrode/electrolyte interface: it is an effect of lower electron transport by carbon, which should foster (de)lithiation process. The $C_{dl}$ is again observed to decrease, because of a smaller electrode surface area after CB agglomeration, while the $Li^+$ ion diffusion coefficient within $LiFePO_4$ seems to not be affected. This could be an indication of almost no degradation occurring in the $LiFePO_4$ lattice. The rise in $R_{ion,L}$ in the infiltrated pores, as shown by the Transmission Line, is not clearly understood, but it may be caused by formation of micropores, with a higher ion resistivity, after LFP cracking and/or increased tortuosity to electrochemically active sites. The most important result from the EIS model is the huge increase in electron resistance $R_{el}$ throughout the CB network, of about two orders of magnitude. This higher resistance correlates with the presence of the non-conducting carbon phase which prevents the electron transfer within the electrode.

## Conclusion

In this work a fresh and a degraded laboratory-made Li-ion battery $LiFePO_4$/C electrode were characterized by impedance spectroscopy (EIS) and low-voltage FIB/SEM analysis to correlate degradation mechanisms to observed loss in capacity.

Modeling of the EIS indicates a large increase with cycling in the electron resistance in the Carbon Black (CB) network in both the aluminum/electrode interface and the electrode/electrolyte interface.

The electron percolation in the CB network was studied with low-voltage FIB/SEM tomography. Low acceleration voltage (1 kV) permitted a detailed study of charging effects in CB agglomerates observed in the aged cathode, indicating that they have a low electronic conductivity.

The presented method combining low-kV SEM in-lens imaging with FIB 3D tomography can yield detailed information about the amount of low-conductivity carbon in aged $LiFePO_4$/C electrodes and we hope the method will prove valuable in failure analysis of battery electrodes, thereby assisting in improving existing and future battery technologies.

## Acknowledgments

The authors gratefully acknowledge financial support from the Danish strategic research council through the project “Advanced Lifetime Prediction of Battery Energy Storage” (contract no. 0603-00589B). The authors wish to thank Ebtisam Abdellahi for laboratory assistance and sample preparation and the Scott Barnett group at Department of Material Science and Engineering at Northwestern University for the assistance in image segmentation and three-dimensional reconstruction.

## References


1. M. Armand, J. M. Tarascon, *Nature*, **451**, 652-657 (2008).
2. B. Scrosati, J. Hassoun, and Y.K. Sun, *Energy Environ. Sci.*, **4**, 3287-3295 (2011).
3. J.M. Tarascon, M. Armand, *Nature*, **414**, 359-367 (2001).
4. A.K. Padhi, K.S. Nanjundaswamy, and J. B. Goodenough, *J. Electrochem. Soc.*, **144**(4), 1188-1194 (1997).
5. Y. Wang, P. He, and H. Zhou, *Energy Environ. Sci.*, **4**, 805-817 (2010).
6. H. Gabrisch, J. Wilcox, M.M. Doeff, *Electrochem. and Solid-State Letters*, **11**, A25-A29 (2008).
7. H.Y.S. Huang, Y.X. Wang, *J. Electrochem. Soc.*, **159**, A815-A821 (2012).
8. D. Wang, X. Wu, Z. Wang, L. Chen, *J. Power Sources*, **140**, 125-128 (2005).
9. M. Zhu, J. Park, A.M. Sastry, *J. Electrochem. Soc.*, **158**, A1155-A1159 (2001).
10. T. Hutzenlaub et al., *Electrochemical and Solid-State Letters*, **15** (3), A33-A36 (2012).
11. M. Ender et al, *J. Electrochem.* Soc., **159**(7), A972-A980 (2012).
12. Z. Liu et al., *J. Power Sources*, **227**, 267-274 (2013).
13. K. Thydén, Y.L. Liu, and J.B. Bilde-Sørensen, *Solid State Ionics*, **178**, 1984-1989 (2008).
14. J. Illig et al, *J. Electrochem. Soc.*, **159**(7), A952-A960 (2012).
15. G. Garcia-Belmonte et al, *Ionics*, **5**, 44 – 51 (1999).
16. R. De Levie, Electrochimica Acta, **9**, 1231-1245 (1964).
17. N. Ogihara, S. Kawauchi, C. Okuda, Y. Itou, Y. Takeuchi, and Y. Ukyo, *J. Electrochem. Soc.*, **159**, A1304-A1309 (2012).
18. R. Younesi et al, *J. Electrochem. Soc.*, **162**(7), A1289-A1296 (2015).
19. G.J. Brug et al, *J. Electroanal. Chem.*, **176**, 275-295 (1984).
20. F. Gao, Z. Tang, *Electrochimica Acta*, **53**, 5071-5075 (2008).
21. J.P. Meyers et al, *J. Electrochem. Soc.*, **147**(8), 2930-2940 (2000).
22. J. Song, M. Bazant, *J. Electrochem. Soc.*, **160**(1), A15-A24 (2013).
23. J. Cazaux, *Microsc. Microanal.*, **10**, 670-684 (2004).
24. D.J. Stokes, *Phil. Trans. R. Soc. Lond. A* **361,** 2771–2787 (2003).
25. J. Sauvola, M. Pietikäinen, *Pattern Recognition*, **33**, 225-236 (2000).
26. T. Kryjak, M. Gorgoń, *Int. J. Appl. Math. Comput. Sci.*, **20**, 571-580 (2010).
27. M. Park et al, *Journal of Power Sources*, **195**, 7904–7929 (2010).
28. R. Scipioni et al, *"Electron Microscopy Investigations of Changes in Morphology and Conductivity of $LiFePO_4$/C Electrodes"*, submitted to *J. Power Sources*.